AGU ADVANCING EARTH AND SPACE SCIENCE

Earth and Space Science

RESEARCH ARTICLE
10.1029/2020EA001371

Temporal and Spatial Impact of Precipitable Water Vapor on GPS Relative Positioning During the Tropical Cyclone Hato (2017) in Hong Kong and Taiwan

Shiwei Yu[1,2] and **Zhizhao Liu**[1,2]

[1]Department of Land Surveying and Geo-Informatics, the Hong Kong Polytechnic University, Kowloon, Hong Kong, [2]Research Institute for Sustainable Urban Development, the Hong Kong Polytechnic University, Kowloon, Hong Kong

Key Points:

- The performance of global positioning system (GPS) positioning is degraded by 255% during the 2017 tropical cyclone Hato
- The Spearman's correlation coefficient between degradation and precipitable water vapor (PWV) variation is 0.65 on average in Hong Kong
- The degrading trend in Hong Kong and Taiwan is 9.86 mm/h and 1.20 mm/h on average when the PWV has a high-dynamic spatial variation

Correspondence to:
Z. Liu,
lszzliu@polyu.edu.hk

Citation:
Yu, S., & Liu, Z. (2021). Temporal and spatial impact of precipitable water vapor on GPS relative positioning during the tropical cyclone Hato (2017) in Hong Kong and Taiwan. *Earth and Space Science*, *8*, e2020EA001371. https://doi.org/10.1029/2020EA001371

Received 4 AUG 2020
Accepted 30 JAN 2021

Abstract The evident disturbance of global positioning system (GPS) positioning results responding to the 2017 tropical cyclone (TC) Hato is observed in both Hong Kong and Taiwan regions. The GPS solutions of 10 baselines, i.e., five from Hong Kong and five from Taiwan, with baseline lengths ranging from 4.8 to 46.6 km, are analyzed during the TC period from August 16 to 26, 2017. The precipitable water vapor (PWV) variation in temporal and spatial domains is also investigated in terms of 2–5 h scale-averaged wavelet power and normalized magnitude of spatial gradient. The results indicate that there is a close correlation between positioning disturbance and the spatiotemporal variation of PWV during the TC period. The daily Spearman's correlation coefficient on TC-impacted day is 0.65 for Hong Kong baselines, ~1.97 times as large as the mean value 0.33 of the non-TC-impacted period. Furthermore, the positioning performance started to degrade when the normalized magnitude of the spatial gradient of PWV experienced a rapid increase. The degradation lasted for ~7 h, and the degrading trend for Hong Kong baselines is 9.86 mm/h on average. For Taiwan baselines, the degradation lasted for ~31 h, and the degrading trend is 1.20 mm/h on average. In addition, the GPS three-dimensional positioning average accuracy on the TC-impacted day, July 22, 2017, degraded by 255% over the 10 baselines with respect to that of the other non-TC-impacted days.

1. Introduction

Atmospheric precipitable water vapor (PWV) plays a crucial role in the Earth's climate (Hanisco et al., 2007; Hegglin et al., 2014; Zahn et al., 2014). It also has especially important effects on regional weather, such as precipitation. In weather forecasts, PWV is an essential meteorological parameter, which is often assimilated into the numerical weather prediction (NWP) models (Andersson et al., 2005; Hoffman & Grassotti, 1996; Lawrence et al., 2018; Mateus et al., 2018; Wang et al., 2018), e.g., the weather research and forecasting (WRF) model developed by the National Center for Atmospheric Research (NCAR), and the integrated forecasting system jointly developed by the European Centre for Medium-Range Weather Forecasts (ECMWF) and Météo-France. Furthermore, PWV content in the atmosphere makes an adverse impact on the propagation of electromagnetic waves (Gordon, 1987; Smith & Weintraub, 1953), particularly on signal transmission between satellites and ground stations, such as global positioning system (GPS) satellites.

GPS is a powerful tool to provide the position service in different applications such as navigation (Li et al., 2019; Zhou & Li, 2017) and subsidence monitoring (Hu et al., 2019; Hwang et al., 2016). The positioning accuracy principally depends on the accuracy of the models used to correct the atmospheric delays, including the troposphere and ionosphere (Han & Wang, 2017; Macalalad et al., 2016; Vaclavovic et al., 2017; Zou et al., 2017). Due to the ionosphere's dispersive property, GPS signals on different frequencies have different time delays (Garbuny, 1965). As a result, ionospheric delay can be canceled by using observations of different frequencies (Blewitt, 1989; Dong & Bock, 1989). Unlike the correction of ionospheric delay, the mitigation of tropospheric effect on GPS signals has to rely on different models instead, such as Saastamoinen (Saastamoinen1972), Hopfield (Hopfield, 1969), and UNB3 (Leandro et al., 2006, 2008). The tropospheric delay of GPS signals is comprised of two parts: One is the hydrostatic component, accounting for ~90%, and the other one is the wet component mainly caused by the water vapor in the atmosphere, accounting for ~10% (Hopfield, 1971). The hydrostatic component can be modeled with high precision (Tregoning & Her-

ring, 2006). However, precise modeling of wet delay is difficult, especially in conditions of severe weather such as tropical cyclones (TCs).

A tropical cyclone is a rapidly rotating storm system with complex weather, such as powerful winds, heavy rainstorms, and damaging thunderstorms (Marks, 2015). With global warming, the intensity of TCs is showing an increasing trend (Bhatia et al., 2019; Emanuel, 2005; Landsea, 2005; Yamaguchi et al., 2020; Zhao et al., 2018). This trend has drawn researchers' attention to study TCs from different aspects, including the dynamics of the water vapor inside and outside TCs. For instance, the circulation of precipitation and water vapor in TCs was discussed by Fudeyasu et al. (2008), Makarieva et al. (2017), and Wang and Hankes (2016). Allison et al. (2018) simulated the vertical transport of water vapor for TC Ingrid (2013). In addition, Won and Kim (2015) analyzed the evolution of PWV along the path of typhoon Ewiniar (2006) in both temporal and spatial domains.

The uncertainty of PWV variation in the atmosphere, in turn, makes it hard to model the atmospheric delay precisely and thus affects GPS precise applications. Dodson et al. (1996), Geiger (1988), and Santerre and Geiger (2018) discussed the impact of the troposphere on the positioning performance, particularly in the up component. The performance of GPS precise point positioning (PPP) with different troposphere models during severe weather conditions was evaluated by Tunalı and Özlüdemir (2019). The augmentation of the PWV-related observations, e.g., in situ and NWP-derived meteorological parameters, can help improve the performance of the GPS positioning in terms of convergence time and accuracy (Lagler et al., 2013; Lu et al., 2016; Wang & Liu, 2019; Wilgan & Geiger, 2018; Wilgan et al., 2017). Previous research has paid a close attention to the refinement of atmospheric modeling in order to improve the GPS positioning precision. However, in extreme cases such as tropical cyclones, the exact correlation between the PWV variation and GPS positioning performance is seldom investigated and it is still not understood.

This research aims to investigate the impact of PWV variation on GPS positioning during the 2017 tropical cyclone Hato. First, the data set, including tropical cyclone information, GPS observations, ECMWF Re-analysis (ERA5), and the temporal and spatial analyzing models, is introduced in Section 2. Then, the relationships between the PWV temporal and spatial variation and positioning deviation are discussed in Section 3. The main conclusions are summarized in Section 4.

2. Data and Method

2.1. 2017 Tropical Cyclone Hato

The 2017 tropical cyclone Hato was the thirteenth tropical cyclone over the western North Pacific and the South China Sea in 2017. It formed as a tropical depression over the western North Pacific about 740 km east-southeast of Kaohsiung, Taiwan, on the night of August 20, 2017. On 22nd August, it intensified into a typhoon after moving through the Luzon Strait. On 23rd August, Hato approached toward the Pearl River estuary, Mainland China and developed into a super typhoon (superT) with winds greater than 185 km/h, the strongest category defined by the Hong Kong Observation (HKO). It made landfall over the coast near Macao and Zhuhai at ~04:50 UT on 23rd August. Finally, Hato moved across Guangxi, Mainland China, on 24th August and dissipated over Yunnan at night (Hong Kong Observatory, 2019). The detailed track of Hato was retrieved from the International Best Track Archive for Climate Stewardship (IBTrACS) of the National Oceanic and Atmospheric Administration (NOAA), as depicted in Figure 1 (Knapp et al., 2010).

To validate the accuracy of ERA5 data used in the following analysis of this study, we retrieved the atmosphere pressure in the ocean area at 00:00 UT on the days of 21st August, 22nd August, and 23rd August, as shown in Figure 2. In addition, the corresponding TC center from the IBTrACS data was displayed. The results show that the locations with the minimum pressure from ERA5 data set is consistent with those of TC center (TC centers normally have the minimum pressure) from the IBTrACS data during the 2017 Hato period. This indicates that the ERA5 data had a good quality and suitable for this analysis.

2.2. GPS Data and Processing

The GPS data used in this study are obtained from the Satellite Positioning Reference Station Network (SatRef) operated by the Lands Department of the Government of Hong Kong Special Administrative Region

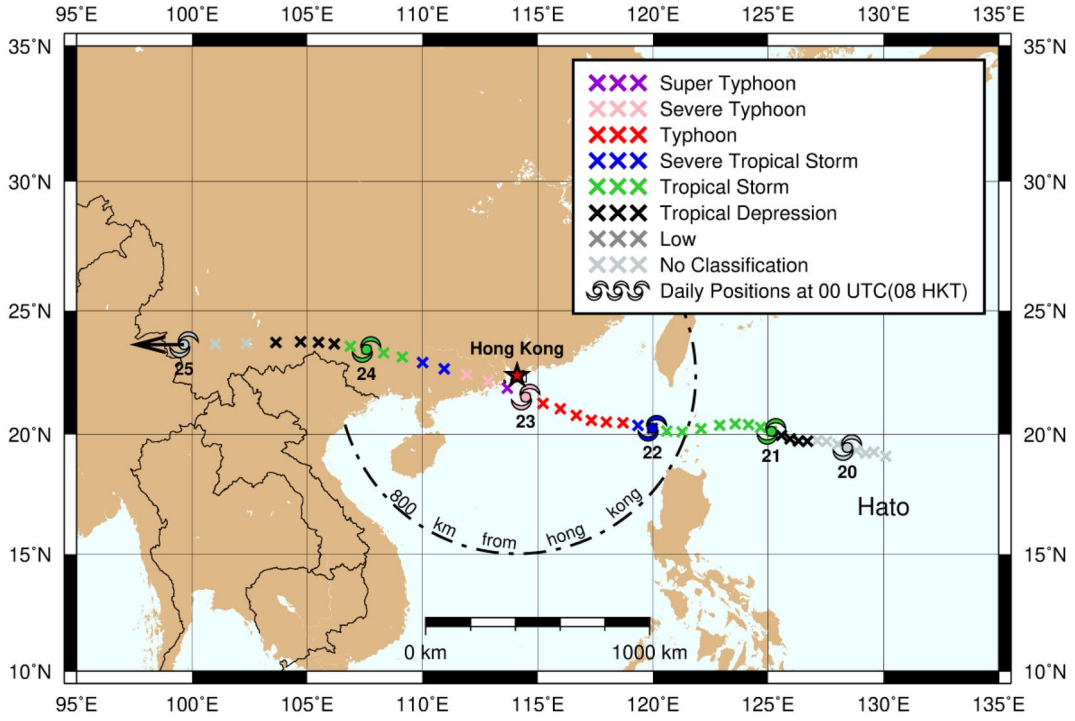

Figure 1. The trajectory of the 2017 tropical cyclone Hato. The intensities are classified into seven categories according to the 10 min average maximum wind speed near the tropical cyclone center. 1. Super Typhoon (SuperT) with wind speed of 185 km/h and above; 2. Severe Typhoon (ST) with wind speed of 150–184 km/h; 3. Typhoon (T) with wind speed of 118–149 km/h; 4. Severe Tropical Storm (STS) with wind speed of 88–117 km/h; 5. Tropical Storm (TS) with wind speed of 63–87 km/h; 6. Tropical Depression (TD) with wind speed of 41–62 km/h; 7. Low (LW) with wind speed of ~40 km/h. The position of TC center along its track is displayed at a 3 h interval. The location of TC center at 00 UTC each day is indicated with the date in August 2017. TC, tropical cyclone.

(HKSAR), and the Global Positioning System Network operated by the Institute of Earth Sciences (IES), Academia Sinica of Taiwan. The spatial distribution of the GPS stations is illustrated in Figure 3. 10 baselines were formed from the stations. They are HKMW-HKPC, HKKT-HKST, HKKT-HKOH, HKSL-HKSS, HKCL-HKWS from the Hong Kong network, and S104-TTSH, ERPN-SHAN, ERPN-TTSH, SHAN-S104, SHAN-TTSH from the Taiwan network, with baseline length of 4.8 km, 13.3 km, 27.5 km, 35.7 km, 46.6 km, 9.2 km, 18.8 km, 21.7 km, 31.9 km, and 40.4 km, respectively. Their reference coordinates were obtained using the GPS Software Bernese in the PPP model (Dach et al., 2015). Then, the baseline pairs were processed in the relative positioning mode using the software of RTKLIB (Takasu, 2011). The processing strategy is summarized in Table 1. It is worthwhile to note that the ionosphere-free combination observations L3 were used to mitigate the ionosphere effects, because previous studies suggested that the tropical cyclones can trigger ionospheric irregularities (Ke et al., 2019; Yang & Liu, 2016).

2.3. GPS-Based PWV

2.3.1. PWV Retrieval from GPS Observations

To get PWV with a high temporal resolution, e.g., 15 min, the zenith wet delay (ZWD) at GPS stations is estimated in PPP mode. After error correction on GPS measurements, such as the phase center offset (PCO) and variation (PCV), phase wind-up, relativistic effect, and site displacements effects (Kouba & Héroux, 2001; Zumberge et al., 1997), the PPP estimation model can be simplified as:

$$P^s_{r,\mathrm{IF}} = \rho^s_r + c \cdot \left(dt_r - dt^s\right) + m^s_r \cdot \left(\mathrm{ZHD}_r + \mathrm{ZWD}_r\right) + e_{\mathrm{IF}} \tag{1}$$

$$\lambda_{\mathrm{IF}}\varphi^s_{r,\mathrm{IF}} = \rho^s_r + c \cdot \left(dt_r - dt^s\right) + m^s_r \cdot \left(\mathrm{ZHD}_r + \mathrm{ZWD}_r\right) + \lambda_{\mathrm{IF}} \cdot N_{\mathrm{IF}} + \varepsilon_{\mathrm{IF}} \tag{2}$$

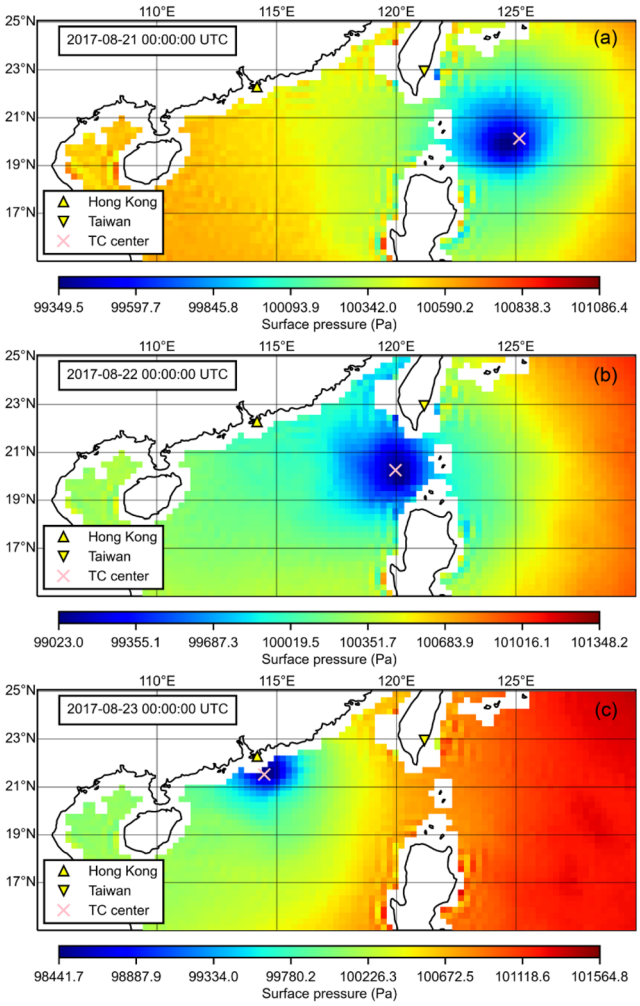

Figure 2. The tropical cyclone Hato's eye center (pink cross) from the IBTrACS data set at 00:00 UT on three days i.e., (a) August 21, 2017, (b) August 22, 2017, and (c) August 23, 2017. The background color represents the surface pressure retrieved from the ERA5 data. It shows that the locations of minimum pressure derived from ERA5 data match very well with those of eye centers derived from IBTrACS data set. The pressure on the land was not shown for the purpose of clear illustration. ERA, ECMWF Re-analysis; IBTrACS, International Best Track Archive for Climate Stewardship.

where $P^s_{r,\mathrm{IF}}$ (m) and $\varphi^s_{r,\mathrm{IF}}$ (cycle) are the ionosphere-free combination observations on pseudorange and carrier phase measurements from the satellite s to the receiver r, respectively; λ_{IF} is the carrier phase wavelength of the ionosphere-free combination; ρ_r^s (m) represents the geometrical distance between the satellite and the receiver; c (m/s) is the speed of light in vacuum; dt_r (second) and dt^s (second) are the clock errors of the receiver and satellite, respectively. ZHD_r and ZWD_r are the two components of the tropospheric delay, i.e., zenith hydrostatic delay which can be precisely obtained from models as mentioned above, and zenith wet delay which usually is estimated along with the coordinates and other parameters, above the GPS receiver. m_r^s is the mapping function, which project the zenith delay into the slant delay in the line-of-sight direction; N_{IF} represents the noninteger ambiguity of ionosphere-free carrier phase combination; e_{IF} (m) and $\varepsilon_{\mathrm{IF}}$ (m) are the relevant measurement noise components on pseudorange and carrier phase measurements, respectively.

Based on the ZWD at the station, the corresponding PWV can be calculated by the following formula (Yeh et al., 2016):

$$\mathrm{PWV} = \mathrm{ZWD} \cdot \Pi \tag{3}$$

where Π is the PWV conversion factor, and can be expressed as (Yeh et al., 2016):

$$\Pi = \frac{10^6}{\rho_w R_w \left(K_2^{'} + K_3 / T_m\right)} \tag{4}$$

where ρ_w (kg/m^3) is the density of liquid water; R_w is the specific gas constant for water vapor; T_m (Kelvin) is the weighted-mean temperature of the atmosphere; $K_2^{'}$ and K_3 are two atmospheric refractivity constants.

In detail, the numerical expression of T_m can be written as (Yeh et al., 2016):

$$T_m = \frac{\int_H^{+\infty} \frac{e(h)}{T(h)} dh}{\int_H^{+\infty} \frac{e(h)}{T(h)^2} dh} \tag{5}$$

where H (m) is the height of the station; $e(h)$ (hPa) is the water vapor pressure at the given height h; $T(h)$ (Kelvin) is the absolute temperature at the given height h; dh (m) is the increment along the vertical integral path.

2.3.2. Scale-Averaged Wavelet Power of Differenced PWV

The continuous wavelet transformation (CWT) was herein utilized to analyze the characteristics of the PWV differences between two GPS stations of each baseline in the time-frequency domain. A time series of PWV difference between two stations was generated. Then, the CWT was applied to the time series thus even small variations can be extracted. The variations revealed by the CWT transformation can help to study GPS positioning disturbances resulting from the abnormal variation of PWV due to the superT.

CWT is a functional approach to investigate the time-varying frequency spectrum characteristics of nonstationary signals (Sadowsky, 1994). The transformation has been widely used for numerous studies in geophysics, including tropical convection (Weng & Lau, 1994), lightning (Larnier et al., 2017), and earthquakes (Sinha et al., 2005). The detailed implementation of the CWT has been described in Liu et al. (2007),

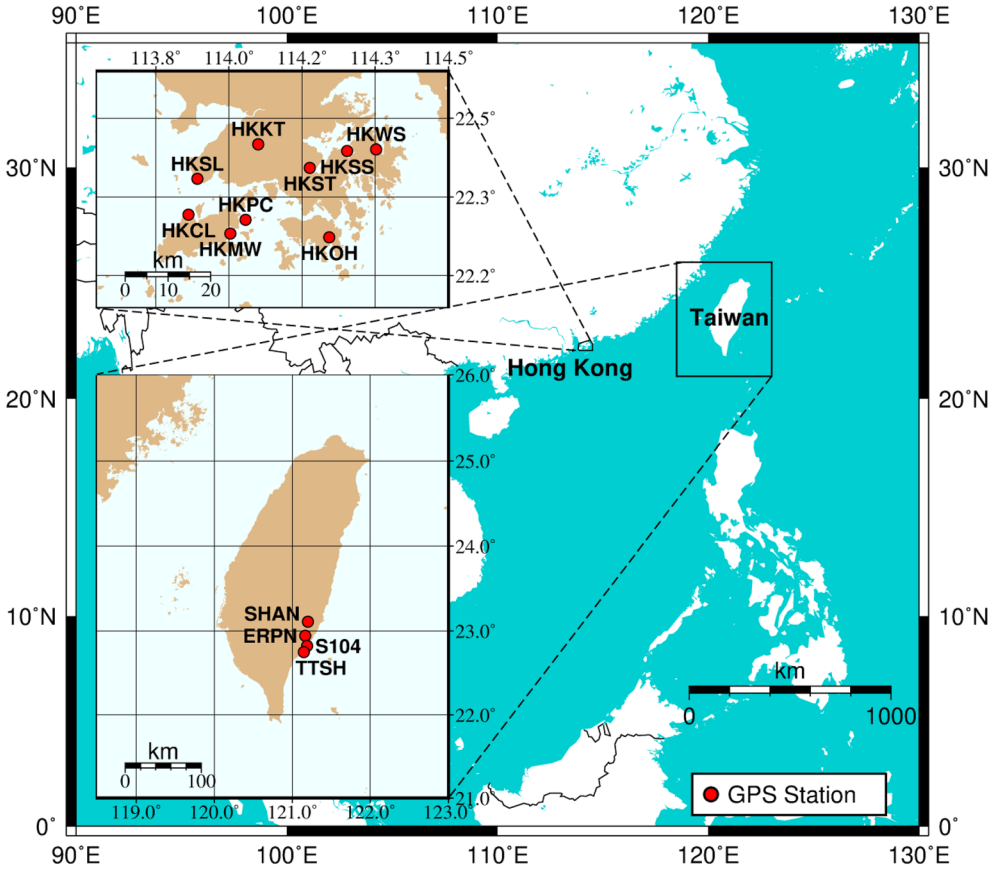

Figure 3. Distribution of the GPS stations in Hong Kong and Taiwan regions. GPS, global positioning system.

Nenadic and Burdick (2005), and Torrence and Compo (1998). The CWT can be simplified as the following expression:

$$W_n(s) = \sum_{k=0}^{N-1} \hat{x}_k \hat{\psi} * (s\omega_k) e^{i\omega_k n \delta t} \tag{6}$$

Table 1
Configuration of GPS Data Processing

Items	Models and strategies
Observations	Pseudorange and carrier phase on GPS L3 ionosphere-free combination observations
Observation weighting	Elevation-dependent weight
Sampling interval	30 s
Elevation mask angle	10°
Satellite orbit	Fixed using the products from the IGS (Dow et al., 2009)
Satellite clock	Fixed using the products from the IGS
Ionospheric delay	First-order effect eliminated by ionosphere-free combination
Tropospheric delay	Estimated with the coordinates
Ambiguity resolve	Estimated as real number
Receiver coordinates	Estimated in the kinematic mode
Filter model	Forward and backward

GPS, global positioning system; IGS, International GPS Service.

$$\omega_k = \begin{cases} \frac{2\pi k}{N\delta t}, k \le \frac{N}{2} \\ -\frac{2\pi k}{N\delta t}, k > \frac{N}{2} \end{cases} \tag{7}$$

where s is the wavelet scale; n is the localized time index; $k = 0...N-1$ is the frequency index; $\hat{x}_k$ is the discrete Fourier transform (DFT) of the observation sequence; $\hat{\Psi}$ is the Fourier transform of the wavelet basis, such as Morlet used in this study; the operator $(*)$ is the complex conjugate; δt is the time step.

Moreover, the power variation over a range of scales was examined by scale-averaged wavelet power, which is defined as the weighted sum of the wavelet power spectrum over scale s_1 to s_2:

$$\bar{W}_n^2 = \frac{\delta j \delta t}{C_\delta} \sum_{j=j_1}^{j_2} \frac{\left|W_n\left(s_j\right)\right|^2}{s_j} \tag{8}$$

$$s_j = s_0 2^{j\delta j}, j = 0,1,\ldots,J \tag{9}$$

$$J = \delta j^{-1} \log_2\left(\frac{N\delta t}{s_0}\right) \tag{10}$$

where s_0 is the smallest resolvable scale and s_J is the largest scale; C_δ is the reconstruction factor of the wavelet basis, e.g., 0.766 for Morlet with frequency of 6; δj is the factor for scale averaging; The other terms have been previously defined.

In addition, a significance test for the scale-averaged wavelet spectrum was applied to determine if the time series has a mean power spectrum. In other words, if a peak in the wavelet power spectrum is significantly larger than this background spectrum, then it can be assumed to be a true feature with a certain confidence coefficient, e.g., the 95% confidence level used in this study (Torrence & Compo, 1998).

2.4. ERA5-Based PWV

2.4.1. PWV Retrieval From ERA5 Product

Although the GPS-based PWV has a high temporal resolution, its spatial resolution is low. Particularly in the marine area, there is no GPS station. But the PWV above the marine area can be retrieved from the ERA5 product (Copernicus Climate Change Service (C3S), 2017), which can facilitate the study of the spatial variation of PWV in both Hong Kong and Taiwan regions. ERA5 is the fifth generation ECMWF atmospheric re-analysis of the global climate (Simmons et al., 2020). Compared with previous generations, the accuracy of ERA5 has been further improved, e.g., global-mean correlation with monthly mean GPCP data was increased from 67% to 77% for precipitation (Hersbach et al., 2020). It provides hourly data on a large number of atmospheric, land, and oceanic climate variables on a global scale. The spatial resolution is 0.25 ° × 0.25 ° in latitude and longitude with 37 pressure levels in the vertical. In addition, ERA5 also provides column-total hourly data, i.e., parameters integrated from the surface to the top of the atmosphere. The product of ERA5 hourly data on single level can be downloaded from website (https://cds.climate.copernicus.eu/cdsapp#!/dataset/reanalysis-era5-single-levels?tab=form) and the PWV data can be directly retrieved from the ERA5 data set. The ERA5-based PWV data on single level used in this study covers the area of 15°N to 25°N, and 112°E to 124°E.

2.4.2. Spatial Gradient of ERA5-Based PWV

The spatial gradient of the ERA5-based PWV is used to investigate the spatial variation of PWV during the TC period in Hong Kong and Taiwan regions. The spatial gradient can be defined as the first-order derivative along the latitude and longitude at a given location:

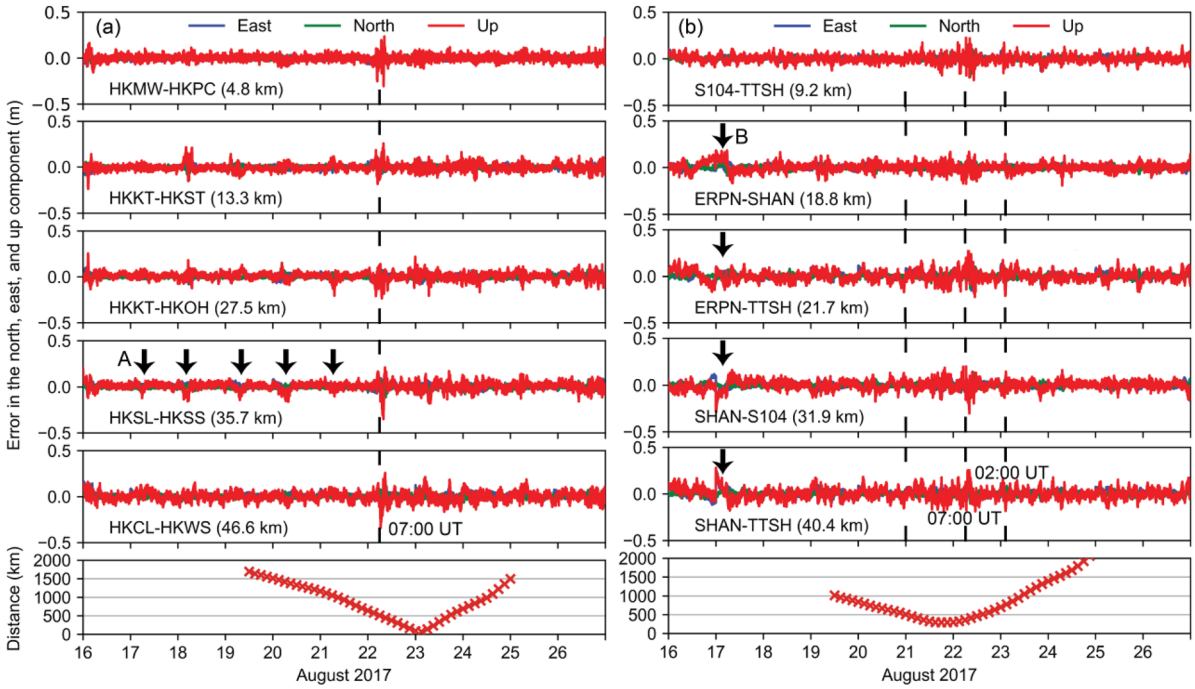

Figure 4. Positioning error (top panels) in the components of east, north, and up of each baseline in Hong Kong (a) and Taiwan (b) regions during the period of Hato. The distances from the center of the tropical cyclone to Hong Kong and Taiwan are shown in (a) and (b) of the bottom panel.

$$\mathrm{PWV}_{grad} = \left[\frac{\partial \mathrm{PWV}(\mathrm{lat},\mathrm{lon})}{\partial \mathrm{lat}}, \frac{\partial \mathrm{PWV}(\mathrm{lat},\mathrm{lon})}{\partial \mathrm{lon}}\right] \tag{11}$$

This formula is derived under the assumption that the PWV has derivatives along the latitude and longitude. The ERA5 data set is generated by a hybrid incremental 4-dimensional variational data assimilation (4D-Var) system via integrated forecasting system with the version of Cycle 41r2, which was operational at ECMWF in 2016 (Hersbach et al., 2019). The linear model in both temporal and spatial domains has been applied to data processing of integrated forecasting system (Courtier et al., 1994). Therefore, we assumed the ERA5-derived PWV has derivatives in the directions of latitude and longitude.

3. Results and Discussions

3.1. Illustration of GPS Positioning Disturbances Responding to the TC

In this section, the performance of GPS positioning during the lifecycle of 2017 tropical cyclone Hato is evaluated from aspects of positioning error in the directions of east, north, and up as shown in Figure 4. Significant positioning disturbances can be clearly observed for baselines in both Hong Kong and Taiwan with the approach of the TC Hato. The disturbance to the baselines in Hong Kong occurred at ~07:00 UT on August 22, 2017, when Hato was ~500 km far from Hong Kong. The disturbance to Taiwan's GPS baselines started at ~00:00 UT on August 21, 2017 and ended at ~07:00 UT on 22nd August. During this period, Hato was passing by Taiwan at the closest distance of ~300 km. After the TC left far away from Taiwan with a distance of ~700 km, the positioning error experienced a slight vibration, which can be observed at ~02:00 UT on 23rd August.

In addition, small and periodical disturbances can be clearly observed at ~07:00 UT every day in the baseline HKSL-HKSS. The periodical disturbances were labeled as A with arrows in Figure 4 (a). Such periodical disturbances can also be captured in other baselines, even though they are not as obvious as those in the baseline HKSL-HKSS. They were probably due to the observation of fewer satellites and poorer geometric distribution (Blanco-Delgado et al., 2017; Meng et al., 2015). The number of observed satellites and the

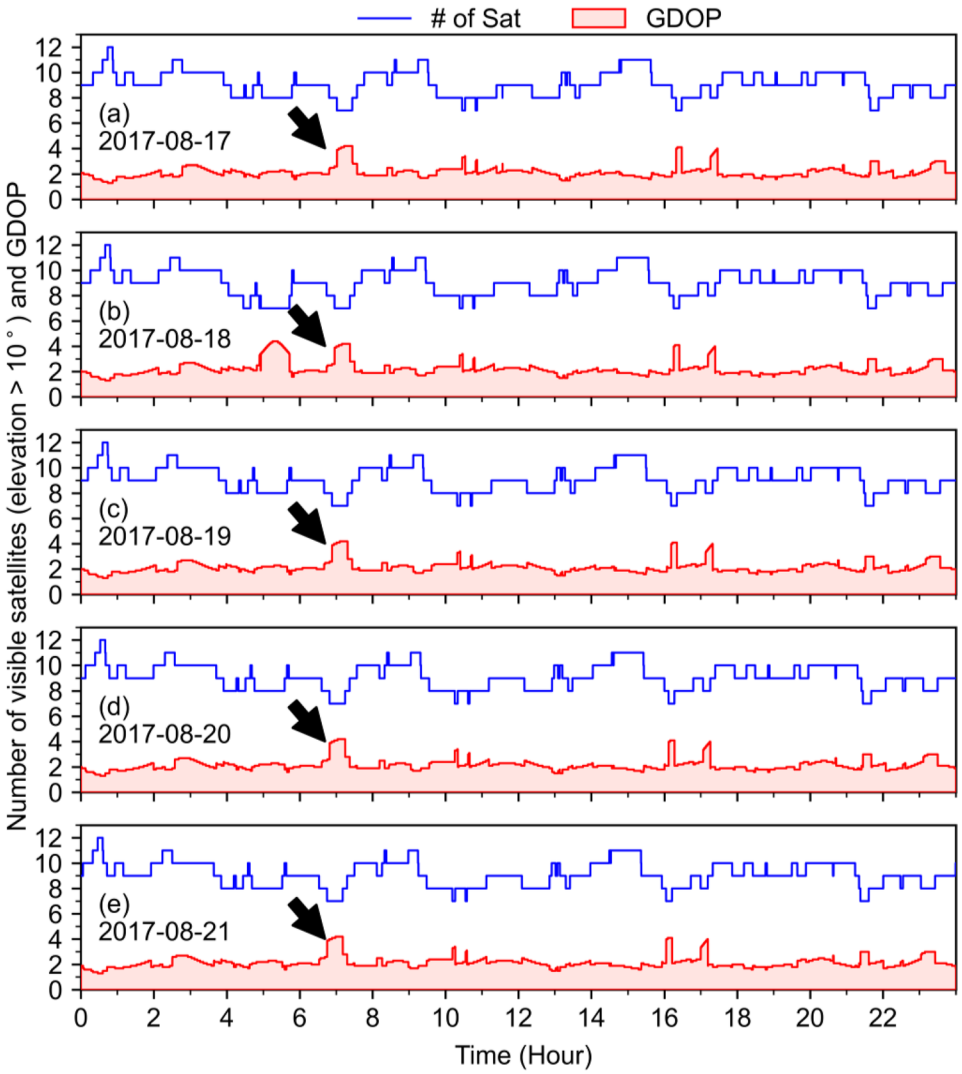

Figure 5. Number of observed satellites with the elevation angle larger than 10° and the GDOP for the GPS station HKSL in Hong Kong from August 17 to 21, 2017. GDOP, geometric dilution of precision; GPS, global positioning system.

geometric dilution of precision (GDOP) of the station HKSL are shown in Figure 5. Around seven satellites at ~07:00 UT every day were visible at station HKSL for a duration of one hour. The GDOP value was ~4, two times larger than the normal value in the other time. On 17 August, there is a large positioning bias for baselines in Taiwan, marked as B with arrows in Figure 4 (b). This bias is not caused by the TC Hato, and the detailed explanation will be provided in the next section.

Figure 6 demonstrates the three-dimensional (3D) positioning error against the TC distance for GPS baselines in Hong Kong and Taiwan. Positive distances indicate that the TC was approaching Hong Kong or Taiwan, and negative values indicate that the TC was leaving these regions. For baselines in Hong Kong, the root mean square (RMS) of positioning error started to increase at ~00:00 UT on 22nd August with the TC distance of ~650 km and reached its peak at ~07:00 UT on 22nd August with the TC distance of ~500 km. When the TC made landfall near Hong Kong with a distance of ~100 km, the RMS positioning error experienced another increase again. For baselines in Taiwan, the RMS positioning error started to increase at ~00:00 UT on 21st August when the TC distance was ~500 km far away from Taiwan. The RMS positioning error reached its peak at ~07:00 UT on 22nd August when the TC was ~ −400 km far from Taiwan. After

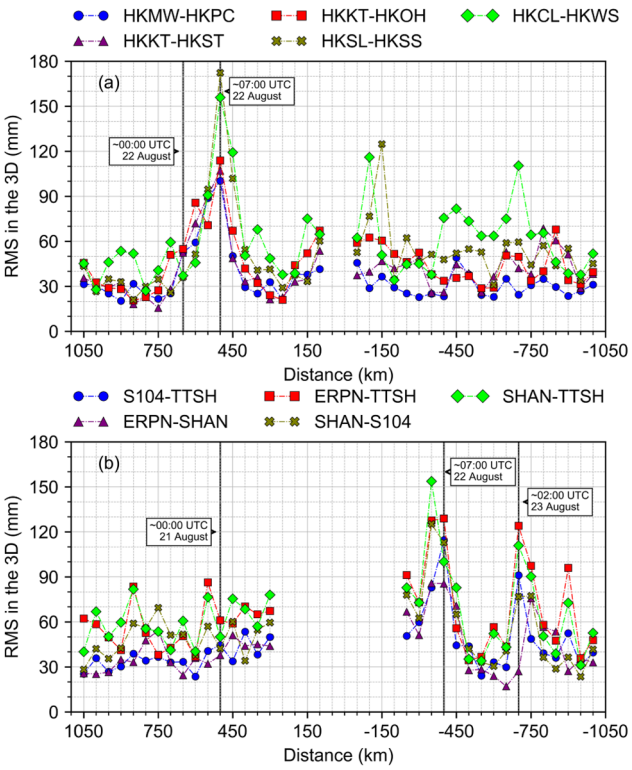

Figure 6. The RMS of positioning error against the distance between Hato and Hong Kong (a) and the distance between Hato and Taiwan (b). Positive distances indicate that the tropical cyclone was approaching Hong Kong or Taiwan, and negative values indicate that the tropical cyclone was leaving these regions. RMS, root mean square.

the TC left away from Taiwan, the RMS positioning error showed another significant increase at the TC distance of ~ −700 km.

3.2. PWV and Differenced PWV Between GPS Stations

To investigate the correlation between the positioning disturbances and the PWV variation over the GPS stations, the corresponding ZWD data were first estimated using the PPP processing model. The estimated ZWD data had a temporal resolution of 15 min. To convert the ZWD into PWV, the weighted-mean temperature in the conversion formula was calculated from the ERA5 hourly pressure level data. Meanwhile, the weighted-mean temperature was linearly interpolated in the temporal domain to ensure that it has the same sampling rate as ZWD. The resultant time series of the PWV at Hong Kong and Taiwan stations are provided in Figure 7 (a) and (b), respectively. It is obvious to note the PWV soared to a high level immediately before the TC passed by Hong Kong and Taiwan. The PWV reached the peak value, i.e., ~70 kg/m^2 when the TC had the closest distance to Hong Kong and Taiwan. Then, it declined gradually when the TC was leaving away. In addition, the PWV retrieved from the ERA5 data set well matched the PWV calculated from GPS stations in Hong Kong during the TC period. Although the PWV from ERA5 was underestimated in the Taiwan region, it followed the same variation trend as that calculated from GPS stations.

Furthermore, the differenced PWV between two stations of each baseline was calculated based on the PWV at each GPS station, as shown in Figure 7 (c)–(l). For the short baselines, i.e., HKMW-HKPC and S104-TTSH , the variation of differenced PWV is very small without significant fluctuation. In contrast, the differenced PWV for long baselines varies significantly with time. Different fluctuation patterns can be observed in the time series of differenced PWV, such as a high-frequency fluctuation marked as arrow A for Hong Kong GPS baselines, and a rapid increase marked as arrow B for Taiwan GPS baselines. The abnormal variation of PWV and its impact on the positioning performance will be further discussed in following sections.

3.3. Scale-Averaged Wavelet Power of GPS-Based Differenced PWV

To further study the PWV impact on the GPS positioning performance under the TC condition, the CWT operation was applied to the time series of differenced PWV. Before the CWT operation, data preprocessing on differenced PWV, including detrending and normalizing, has been carried out to remove the linear trend and scale effect. The detrending processing can be described as:

$$\mathrm{PWV}_d(t) = \mathrm{PWV}(t) - \widehat{\mathrm{PWV}}(t) \tag{12}$$

$$\widehat{\mathrm{PWV}}(t) = a \cdot t + b \tag{13}$$

where $\mathrm{PWV}_d(t)$ is the detrended PWV at time t; $\mathrm{PWV}(t)$ is the original observation sequence; $\widehat{PWV}(t)$ is the linear regression using least squares.

The normalizing formula can be expressed as:

$$\mathrm{PWV}_n(t) = \frac{\mathrm{PWV}_d(t)}{S} \tag{14}$$

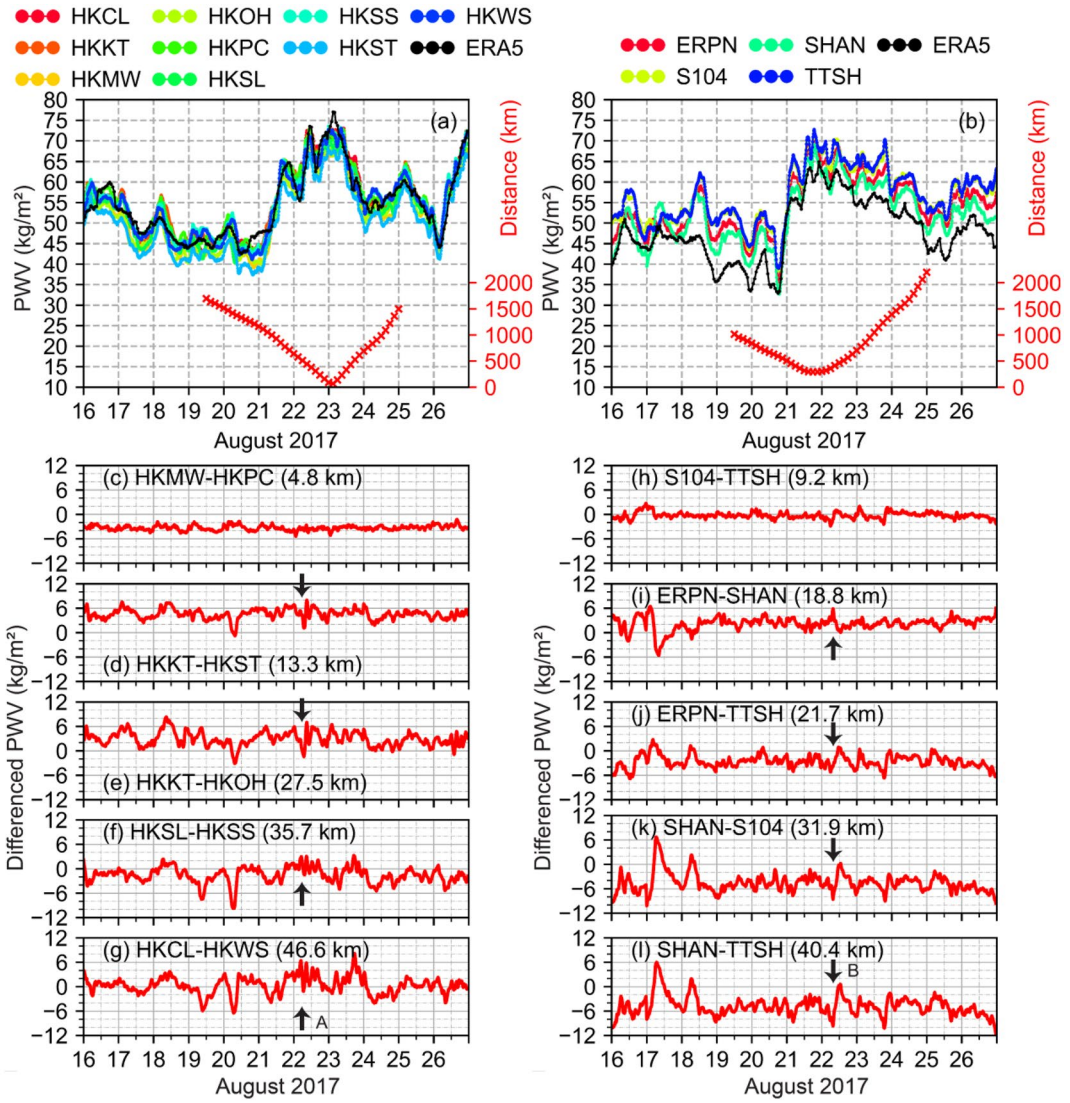

Figure 7. The PWV evolution during the TC period as observed by Hong Kong stations (a) and Taiwan stations (b). The differenced PWV between two GPS stations of each baseline for Hong Kong (c) to (g), and Taiwan (h–l). PWV, precipitable water vapor; TC, tropical cyclone.

where $PWV_n(t)$ is the normalized PWV at time t; S is the standard deviation of the detrended PWV.

After data preprocessing, the scale-averaged wavelet power was calculated to investigate the changing pattern of the differenced PWV. The determination of the time scale was made based on the structure of TCs. The spiral band structure in the vicinity of TCs has a breadth of tens of kilometers on average (Subrahmanyam et al., 2018; Yu et al., 2018). The bands propagate outward in the form of waves along the radial direction for a period of several hours (Nolan & Zhang, 2017; Shi et al., 2020). Accordingly, the 2–5 h scale was herein selected.

In Figure 8, the 2–5 h scale-averaged wavelet power of differenced PWV for 10 GPS baselines is demonstrated. Different changing patterns for baselines in Hong Kong and Taiwan can be observed. There is a significant pulse at ~07:00 UT on August 22, 2017 for baselines in Hong Kong, i.e., HKKT-HKST, HKKT-HKOH, HKSL-HKSS, and HKCL-HKWS. The peak values of the four baselines are 0.89, 1.04, 0.61, and 1.19, much larger than the mean power spectrum with the 95% confidence level, i.e., 0.10, 0.14, 0.14, and 0.18. However, this apparent increase does not appear in the baseline HKMW-HKPC because of its short length (only 4.8 km), in which the spatial correlation at two GPS stations is strong (Ahn et al., 2006; Lawrence

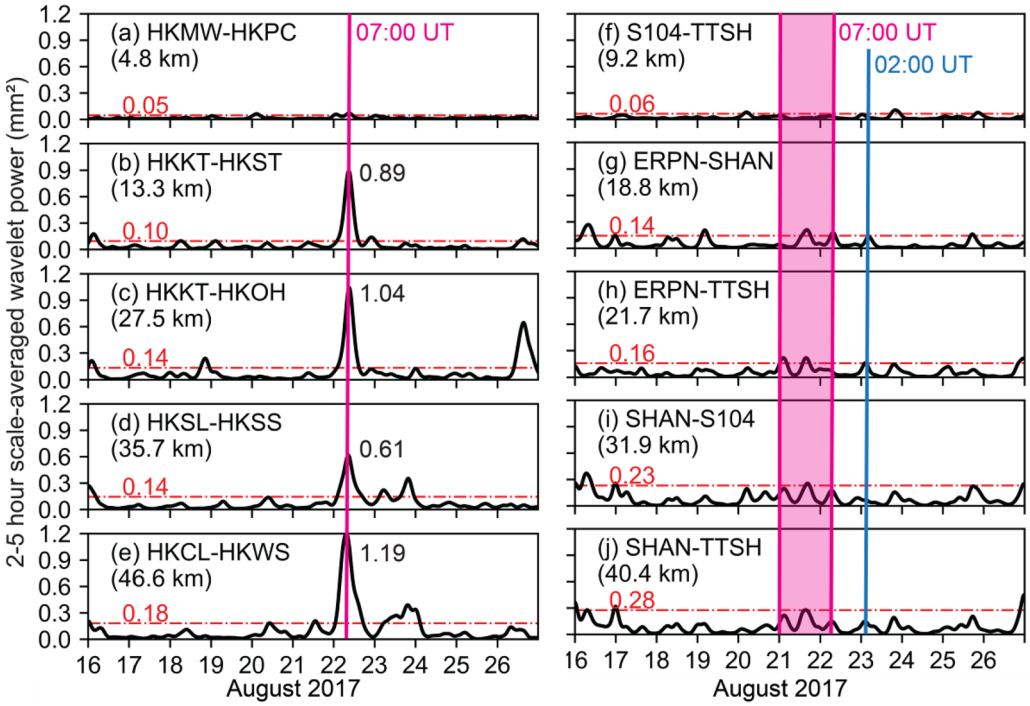

Figure 8. 2–5 h scale-averaged wavelet power of differenced PWV between two GPS stations of each baseline in Hong Kong (a–e), and Taiwan (f–j). The red dot-dashed line denotes a mean power spectrum with 95% confidence level. The vertical pink line in (a–e) denotes the time of 07:00 UT on 22nd August, when the wavelet power reached the peak. The pink area from 00:00 UT on 21st August to 07:00 UT on 22nd August denotes the period when PWV experienced the abnormal variation in Taiwan. In addition, the blue line (f–j) denotes another increase of wavelet power at 02:00 UT on 23rd August in Taiwan. GPS, global positioning system; PWV, precipitable water vapor.

et al., 2006; Wielgosz et al., 2011). This pulse indicates there was a distinct variation of PWV at ~07:00 UT on 22nd August, when Hong Kong was right in the affected radius of the TC.

In comparison, the scale-averaged wavelet power for baselines in Taiwan has a more stable variation without significant increase. The mean power spectra of the five baselines are 0.06, 0.14, 0.16, 0.23, and 0.28, respectively, slightly larger than those of baselines in Hong Kong. Although there was no significant increase, the slight fluctuation between 21st and 22nd August could still be observed in the baselines, ERPN-SHAN, ERPN-TTSH, SHAN-S104, and SHAN-TTSH except the shortest baseline S104-TTSH. In addition, a small increase of wavelet power for all the baselines occurred at ~02:00 UT on 23rd August.

3.4. Normalized Magnitude of Spatial Gradient of ERA5-Based PWV

To study the impact of the spatial variation of PWV on the GPS positioning performance, the PWV covering the area of 15°N to 25°N and 112°E to 124°E has been retrieved from the ERA5 data set. Based on the ERA5-based PWV, the normalized magnitude of spatial gradient of PWV is established and defined as:

$$\mathrm{PWV}\left(\mathrm{lat},\mathrm{lon}\right)_{\mathrm{norm}} = \frac{\left|\overrightarrow{\mathrm{PWV}}\left(\mathrm{lat},\mathrm{lon}\right)\right|}{\max\left(\mathrm{PWV}\left(\mathrm{lat},\mathrm{lon}\right)\right)} \tag{15}$$

where max (PWV(lat,lon)) is the maximum PWV during the whole period at a location with given latitude and longitude; $\overrightarrow{PWV}\left(lat,lon\right)$ is the gradient vector of PWV at the same location; The operator $|\cdot|$ denotes the norm of a vector.

The normalized magnitude of the spatial gradient of PWV on August 20, 2017 and August 22, 2017 was calculated and shown in Figure 9 and Figure 10, respectively. The first band with strong normalized magnitude

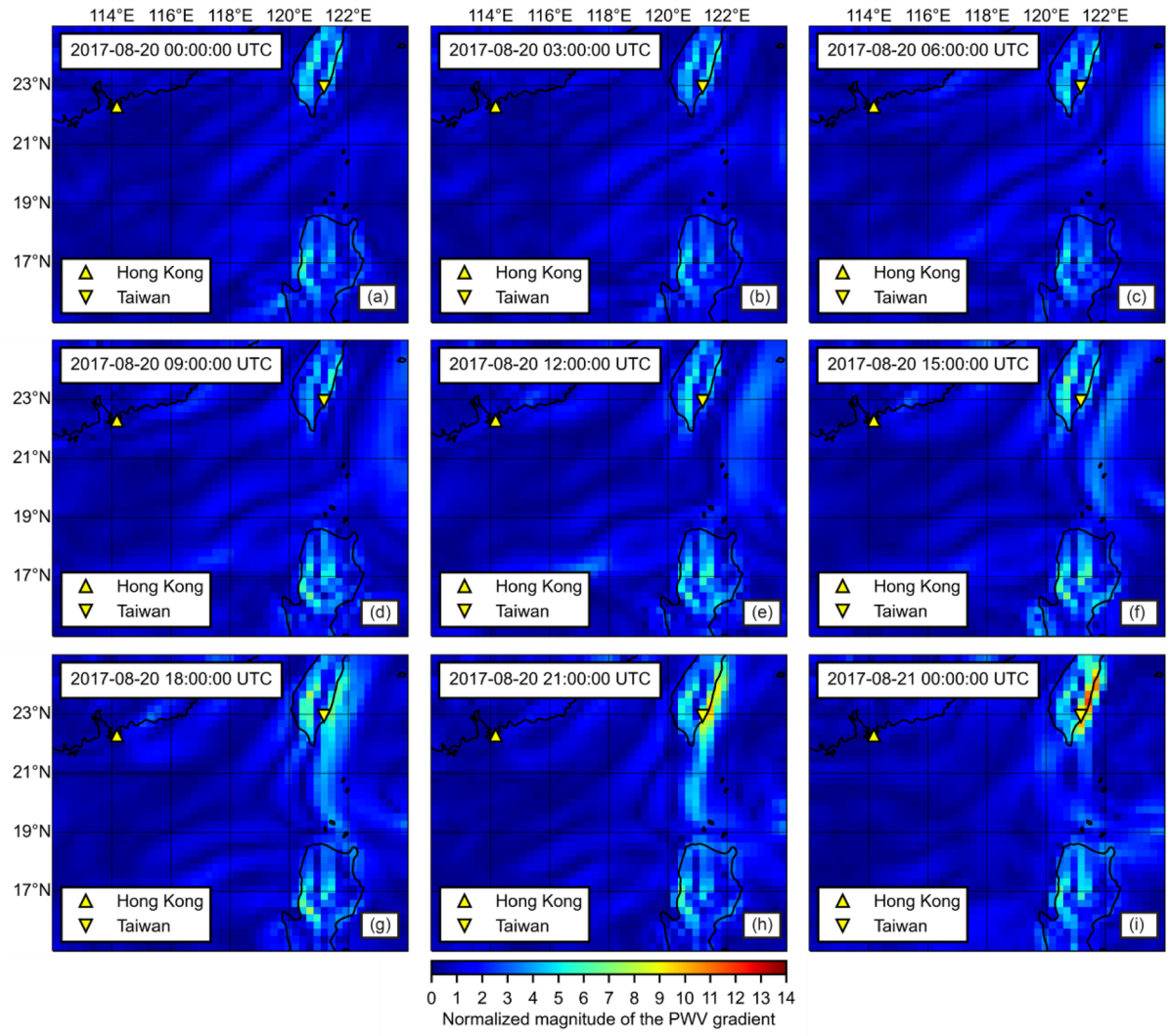

Figure 9. Normalized magnitude of the spatial gradient of PWV in Hong Kong and Taiwan regions on August 20, 2017. On this day, the tropical cyclone center was out of the study area thus it was not shown. PWV, precipitable water vapor.

of PWV spatial gradient started to hit the east coast of Taiwan island at ~18:00 UT on August 20, 2017, when the TC center was ~600 km far away from Taiwan. The normalized magnitude above the GPS stations was 4.749 on average. Five hours later, it increased considerably to a value of 10.556. When the first band with large PWV spatial gradient hit Hong Kong region at ~00:00 UT on 22nd August, the TC was ~650 km far away from Hong Kong. The normalized magnitude above the GPS stations is 1.936 on average, ~2 times as large as the average value of 0.999, just three hours before the first band with large PWV spatial gradient hit Hong Kong. The normalized magnitude in Hong Kong varied afterward as we could see several bands with strong PWV spatial gradient hit Hong Kong continuously.

The normalized magnitude in Hong Kong was smaller than that in Taiwan. That was primarily due to the different terrains of Hong Kong and Taiwan (Bao et al., 2017; Wang et al., 2020; Yeh et al., 2016). The east coast of Taiwan is mountainous, which blocks most of PWV flux from the sea. Although Hong Kong is also a mountainous region, the mountains are not as continuous as Taiwan does. Thus, we presume that the PWV flux cannot be blocked as effectively as over Taiwan, which helps explain these results.

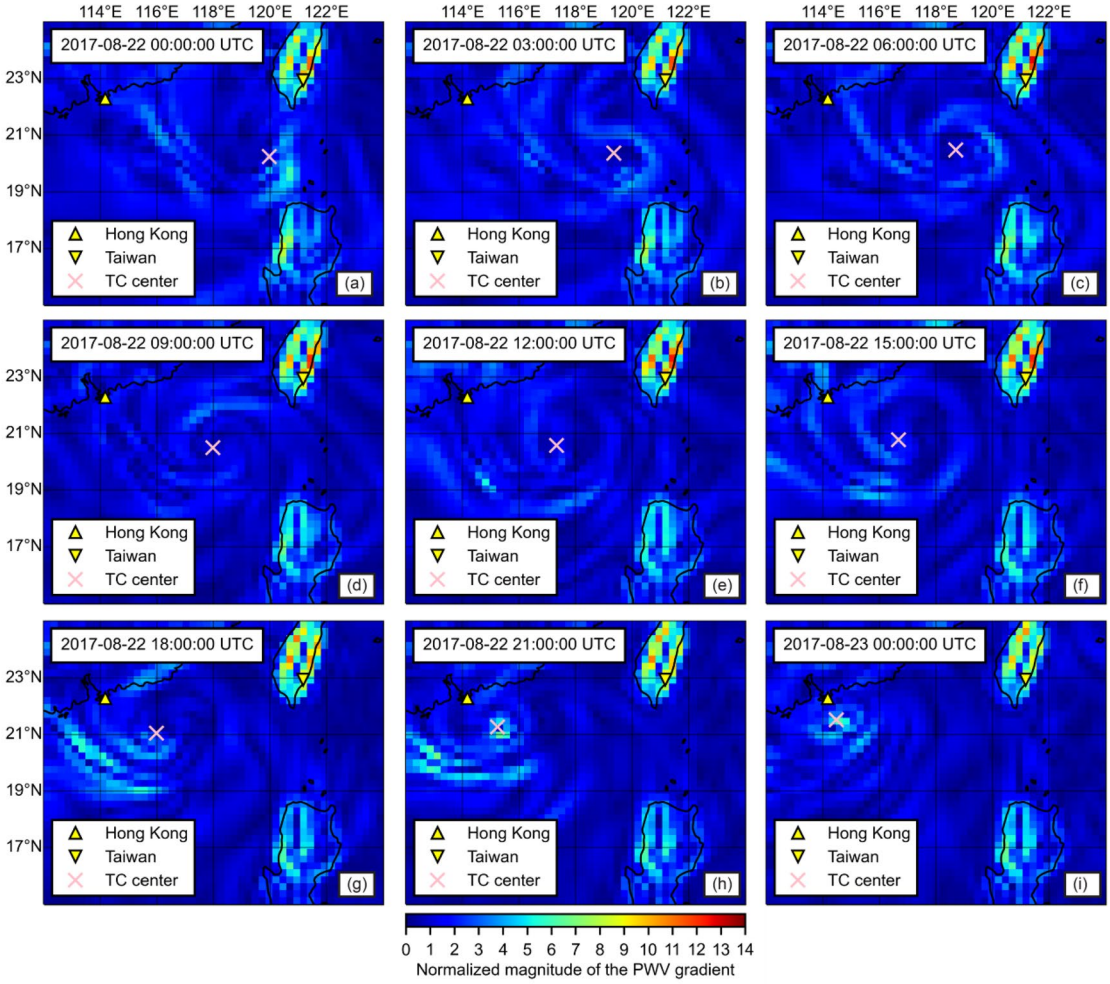

Figure 10. Normalized magnitude of the spatial gradient of PWV in Hong Kong and Taiwan regions on August 22, 2017. PWV, precipitable water vapor.

3.5. Relationship Between Scale-Averaged Wavelet Power of Differenced PWV and GPS Baseline Positioning Error

To investigate the correlation between the 2 and 5 h scale-averaged wavelet power of differenced PWV and GPS baseline positioning error in the same scale, the scaling function was applied to scale-averaged wavelet power using the equation as:

$$\text{power}_{\text{std}} = \frac{\text{power} - \min(\text{power})}{\max(\text{power}) - \min(\text{power})} \tag{16}$$

$$\text{power}_{\text{scaled}} = \text{power}_{\text{std}} \times \left[\max(\text{RMS}) - \min(\text{RMS})\right] + \min(\text{RMS}) \tag{17}$$

where power denotes the 2–5 h scale-averaged wavelet power; RMS denotes the root mean square error of the three dimensional position; and $\text{power}_{\text{std}}$ and $\text{power}_{\text{scaled}}$ represent the standardized and scaled power, respectively.

The results for the baselines in Hong Kong and Taiwan are shown in Figure 11. In the Hong Kong results, one sharp peak in the scaled power of differenced PWV, denoted as red curve in the plots, is observed at all the five baselines. Correspondingly, one sharp peak in GPS baseline positioning error, denoted as

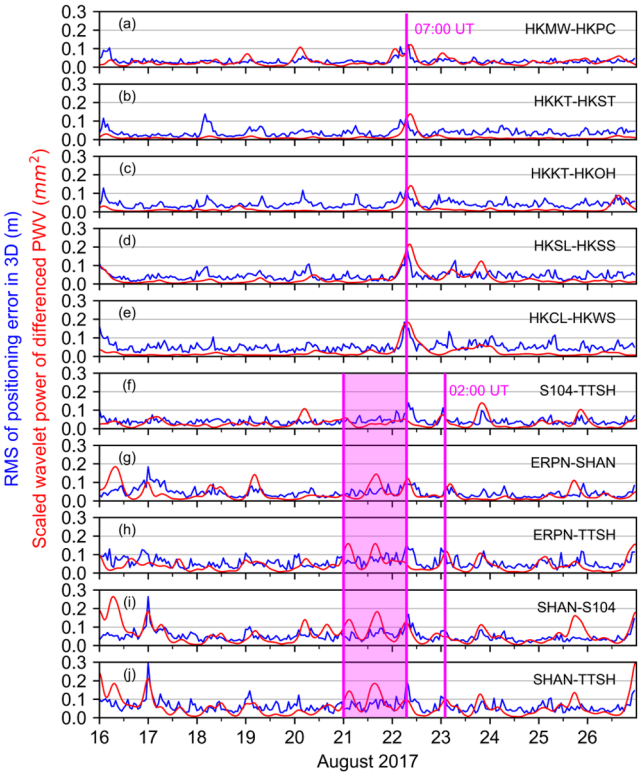

Figure 11. Scaled wavelet power of differenced PWV and RMS of GPS positioning error in the three dimensional component for the baselines in Hong Kong (a–e) and Taiwan (f–j). The vertical pink line at 07:00 UT on 22nd August denotes the time when the RMS positioning error reached the peak in Hong Kong. The pink area denotes the period from 00:00 UT on 21st August to 07:00 UT on 22nd August when PWV experienced the abnormal variation in Taiwan. In addition, the third vertical line at 02:00 UT on 23 August denotes another RMS positioning error increase in Taiwan. GPS, global positioning system; PWV, precipitable water vapor; RMS, root mean square.

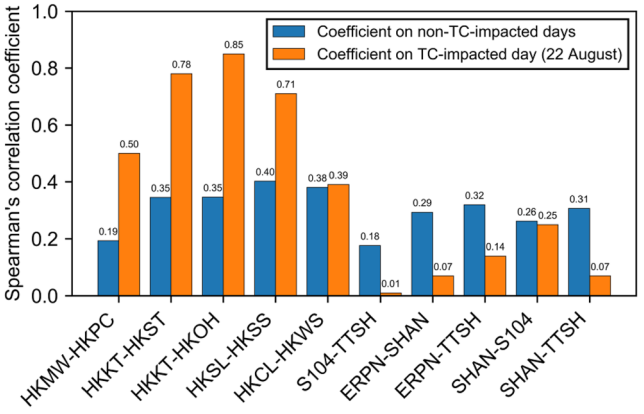

Figure 12. Mean Spearman's correlation coefficient over the non-TC-impacted period (August 16–26, 2017, excluding 22nd August) and the coefficient on the TC-impacted day of 22nd August 2017 for baselines in Hong Kong and Taiwan. TC, tropical cyclone.

blue curve, occurs at the same time. All the peaks occurred at ~07:00 UT on August 22, 2017. The scaled power is 0.08, 0.11, 0.10, 0.18, and 0.18 for HKMW-HKPC, HKKT-HKST, HKKT-HKOH, HKSL-HKSS, and HKCL-HKWS, respectively. The corresponding RMS positioning errors are 0.068 m, 0.135 m, 0.141 m, 0.215 m, and 0.131 m, respectively.

The same general pattern of the scaled power and positioning error can be observed in Taiwan baselines at ~00:00 UT on 17th August, at ~07:00 UT on 22nd August, and at ~02:00 UT on 23rd August. At 00:00 UT on 17th August, there was a reasonable agreement between the RMS positioning error and scaled power of the baselines. For ERPN-SHAN, SHAN-S104, and SHAN-TTSH, the RMS positioning errors were 0.184 m, 0.264 m, and 0.298 m, and the scaled powers were 0.10, 0.18, and 0.21, respectively. It should be noted that this qualitative association between RMS positioning error and scaled power corresponds with the positioning disturbances marked as B in Figure 4 (b). The second correlated variation occurred at the end of abnormal variation of PWV, i.e., ~07:00 UT on 22nd August. The RMS positioning errors were 0.086 m, 0.089 m, 0.159 m, 0.143 m, and 0.207 m for S104-TTSH, ERPN-SHAN, ERPN-TTSH, SHAN-S104, and SHAN-TTSH, respectively. The corresponding scaled powers were 0.05, 0.12, 0.05, 0.13, and 0.10, respectively. In addition, the third correlation can be observed at ~02:00 UT on 23rd August. The value of scaled power is smaller than those of the other two matches and it corresponds to the large RMS positioning error at ~ -700 km in Figure 6 (b).

To further investigate the exact correlation between the wavelet power of differenced PWV and the GPS baseline positioning error, the daily Spearman's rank-order correlation coefficient was calculated using the following equation (Zwillinger, 2002):

$$r_s = 1 - \frac{6\sum d_i^2}{n\left(n^2 - 1\right)} \tag{18}$$

where d_i is the difference in paired ranks; and n is the number of samples.

The averaged correlation coefficient over the non-TC-impacted period from August 16 to 26, excluding 22nd August, and the coefficient on the TC-impacted day of 22nd August are shown in Figure 12. The classification of the correlation coefficient is provided in Table 2. In the non-TC-impacted period, the correlation between the wavelet power of differenced PWV and positioning error is low for both Hong Kong and Taiwan baselines, with mean coefficients ranging from 0.18 to 0.40. However, on the TC-impacted day, the Hong Kong baselines had much higher correlations ranging from 0.39 to 0.85. The daily correlations on 22nd August for the Taiwan baselines are very low, with the coefficients ranging from 0.01 to 0.25.

3.6. Relationship Between Normalized Magnitude of the Spatial Gradient of PWV and GPS Baseline Positioning Error

The normalized magnitude of spatial gradient of PWV above all the GPS stations was calculated to investigate the correlation between the spatial variation of PWV and GPS baseline positioning error. The normalized magnitude is shown as the red curve in Figure 13, and the RMS of GPS baseline positioning error is shown as the blue curve. The mean

Table 2
Rule of Thumb for Interpreting Spearman's Correlation Coefficient (from Akoglu, 2018)

Size of correlation	Interpretation
0.9–1.0	Very high
0.7–0.9	High
0.5–0.7	Moderate
0.3–0.5	Low
0.0–0.3	Negligible

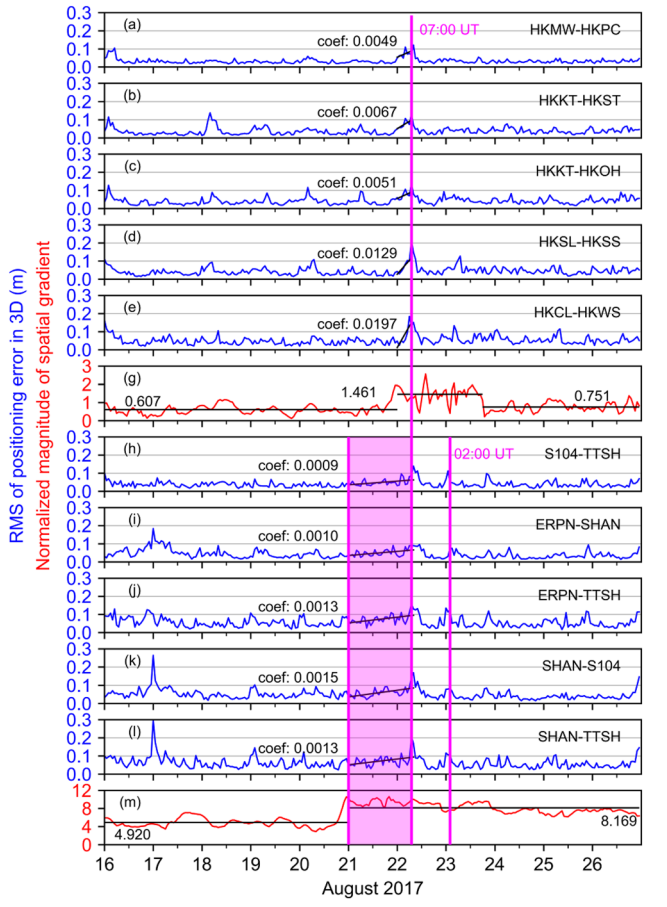

Figure 13. The RMS of GPS positioning three dimensional error for baselines for Hong Kong (a–e) and Taiwan (h–l), and normalized magnitude of the spatial gradient of PWV above all the GPS stations in Hong Kong (g) and Taiwan (m). The normalized magnitude is represented as red curves, and the RMS positioning error is represented as blue curves. The increase trend is represented by the coefficient of the linear regression function of $\mathbf{y} = \mathbf{coef} \cdot \mathbf{x} + \mathbf{b}$. The vertical pink lines and area have the same meaning as in Figure 11. GPS, global positioning system; PWV, precipitable water vapor; RMS, root mean square.

magnitude in Hong Kong region during the whole period is 0.785, which is significantly lower than the mean value 6.690 in Taiwan.

The normalized magnitude started to increase at ~00:00 UT on 22nd August and hovered at a high level until ~18:00 UT on 23rd August. During this period, TC Hato was approaching and made a landfall in Hong Kong, and the normalized magnitude of spatial gradient of PWV experienced an unstable variation. The mean magnitude is 1.461, ~2 times larger than the mean value before and after that period, i.e., 0.607 and 0.751. In terms of the positioning error, the RMS positioning error started to increase at ~00:00 UT, and reached the peak at ~07:00 UT on 22nd August. The increase trend is 4.9 mm/h, 6.7 mm/h, 5.1 mm/h, 12.9 mm/h, and 19.7 mm/h for HKMW-HKPC, HKKT-HKST, HKKT-HKOH, HKSL-HKSS, and HKCL-HKWS, respectively.

For the Taiwan area, the normalized magnitude in Taiwan began to increase at ~00:00 UT on 21st August, when Hato was hitting the east coast of Taiwan. It stayed at a high level, i.e., ~10, for the following days with only a slight decline. The mean magnitude after the sudden increase is 8.169, ~1.67 times as large as the mean value 4.920 before the increase. After the sudden increase of the magnitude, the positioning performance continued to be degraded until ~07:00 UT on 22nd August. The degrading trend is 0.9 mm/h, 1.0 mm/h, 1.3 mm/h, 1.5 mm/h, and 1.3 mm/h for S104-TTSH, ERPN-SHAN, ERPN-TTSH, SHAN-S104, and SHAN-TTSH, respectively.

To further evaluate the GPS positioning performance when the normalized magnitude had a high level, the degradation percentage is calculated using the equation:

$$\text{degradation percentage} = \frac{\text{RMS}_{\text{peak}} - \text{RMS}_{\text{mean}}}{\text{RMS}_{\text{mean}}} \times 100 \quad (19)$$

where RMS_{peak} represents the maximum of the RMS positioning error at ~07:00 UT on August 22, 2017 for both Hong Kong and Taiwan regions; RMS_{mean} is the averaged RMS positioning error over the non-TC-impacted period from August 16 to 26, 2017, excluding 22nd August.

The mean and peak RMS of GPS baseline positioning error for baselines in Hong Kong and Taiwan are shown in Figure 14. The mean RMS positioning error on the non-TC-impacted days is approximately 44 mm on average, ranging from 30 to 60 mm. The peak RMS positioning error on the TC-impacted day has large values ranging from 96 to 215 mm, approximately 156 mm on average. The averaged degradation percentage over these 10 baselines is 255%. This indicates that the TC Hao had a significant influence on the GPS positioning performance, and the performance started to be degraded for baselines in Hong Kong and Taiwan when the magnitude of spatial gradient of PWV experienced a rapid increase.

4. Conclusions

During the 2017 TC Hato, the PWV and GPS positioning performance in both Hong Kong and Taiwan experienced significant variations. Our analysis showed that performance of GPS positioning in both Hong Kong

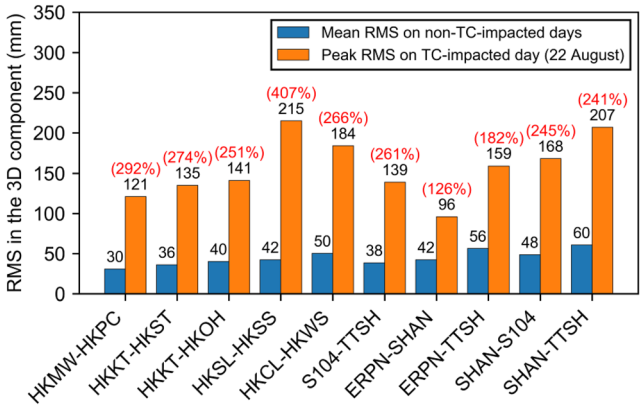

Figure 14. Mean and peak RMS of the GPS baseline positioning error in the three dimensional component for 10 baselines in Hong Kong and Taiwan. The mean RMS positioning error is calculated by averaging the RMS positioning error of each baseline over the non-TC-impacted period from August 16 to 26, 2017, excluding 22nd August. The peak RMS positioning error represented the largest RMS positioning error at ~07:00 UT on August 22, 2017. The degradation percentage of each baseline is labeled as the red value in parentheses. GPS, global positioning system; PWV, precipitable water vapor; RMS, root mean square; TC, tropical cyclone.

and Taiwan was adversely affected by the PWV variations resulting from the TC Hato.

When the TC was ~500 km far away from Taiwan at ~00:00 UT on August 21, 2017, it brought rich PWV to the east coast of Taiwan. The PWV above the GPS stations in Taiwan became more unpredictable due to its high-dynamic variation in temporal and spatial domains, leading to the performance degradation of GPS baseline positioning. After the TC left from Taiwan and was ~500 km away, the performance of GPS baseline positioning came back to normal level.

When the TC approached Hong Kong and was at a distance of ~650 km at ~00:00 UT on 22nd August, TC Hato began to impact Hong Kong, and the PWV showed unstable variations in the both temporal and spatial domains. As a result, the positioning performance started to degrade. When the TC made the landfall at ~4:00 UT on 23rd August, the PWV varied in a different pattern, which resulted in the positioning disturbances again. The positioning performance returned to normal level after the TC left Hong Kong.

In summary, the high-dynamic variation of PWV in temporal and spatial domains, which was triggered by the invasion of the 2017 TC Hato, led to significant disturbances to the GPS positioning performance in Hong Kong and Taiwan regions.

(1) There is a high correlation between wavelet power of time series of differenced PWV and RMS of positioning error in the three dimensional component for baselines in Hong Kong on 22nd August. The daily Spearman's correlation coefficient is 0.50, 0.78, 0.85, 0.71, and 0.39 for baselines HKMW-HKPC, HKKT-HKST, HKKT-HKOH, HKSL-HKSS, and HKCL-HKWS, respectively. Although the daily coefficient for baselines in Taiwan is small, the instantaneous correlation is strong at ~07:00 UT on 22nd August

(2) With the approach of the TC toward Hong Kong and Taiwan, the normalized magnitude of spatial gradient of PWV started to increase. At the same time, the positioning performance began to degrade, and RMS positioning error began to increase. The RMS positioning error increase trend is 4.9 mm/h, 6.7 mm/h, 5.1 mm/h, 12.9 mm/h, and 19.7 mm/h for baselines HKMW-HKPC, HKKT-HKST, HKKT-HKOH, HKSL-HKSS, and HKCL-HKWS, respectively. For the baselines in Taiwan, the RMS positioning error increase trend is 0.9 mm/h, 1.0 mm/h, 1.3 mm/h, 1.5 mm/h, and 1.3 mm/h for S104-TTSH, ERPN-SHAN, ERPN-TTSH, SHAN-S104, and SHAN-TTSH, respectively. The average degradation percentage is 255% for the 10 baselines when compared to the mean RMS positioning error during the non-TC-impacted period from August 16 to 26, (excluding 22nd August) 2017

Data Availability Statement

For feasibility, the data used in this study have been uploaded to the public domain repository, i.e., Figshare, which is a free data repository open to the public. The daily GPS data in the format of Receiver Independent Exchange Format (RINEX) 2.11 during the period from August 16 to 26, 2017 can be download from https://doi.org/10.6084/m9.figshare.12781808.v1. The GPS satellites' daily precise orbit (.sp3) and clock (.clk_30s) products can be downloaded from https://doi.org/10.6084/m9.figshare.12782075.v1. The records of the tropical cyclone Hato 2017 can be downloaded from https://doi.org/10.6084/m9.figshare.12781820.v1. The total column water vapor of ERA5 hourly data on single level ranging from 15°N to 25 N and 112 E to 124 E in latitude and longitude during the period from August 16 to 26, 2017 can be downloaded from https://doi.org/10.6084/m9.figshare.12781778.v1.

Acknowledgments
The grant support from the Key Program of the National Natural Science Foundation of China (project No.: 41730109) is acknowledged. The grant supports from the Hong Kong Research Grants Council (RGC) projects (B-Q61 L PolyU 152222/17E) are highly appreciated. The support from the project (No. 1-BBWJ) in the Emerging Frontier Area (EFA) Scheme of Research Institute for Sustainable Urban Development (RISUD) of The Hong Kong Polytechnic University is also acknowledged. All data are publicly available and free of charge. The Lands Department of the Government of Hong Kong Special Administrative Region (https://www.geodetic.gov.hk/en/rinex/downv.aspx) and the Institute of Earth Sciences (IES) of the Academia Sinica of Taiwan (http://gdbweb.earth.sinica.edu.tw/gps/index.php?pg=1) are acknowledged for providing the GPS data. The International GNSS Service (IGS) is acknowledged for providing the GPS satellites' daily precise orbit and clock products from the ftp address ftp://cddis.gsfc.nasa.gov/gps/products/during the period of August 16–26, 2017. The National Oceanic and Atmospheric Administration (NOAA) is also acknowledged for providing the International Best Track Archive for Climate Stewardship (IBTrACS) data on the tropical cyclones (https://www.ncei.noaa.gov/data/international-best-track-archive-for-climate-stewardship-ibtracs/v04r00/access/csv/). In addition, the European Center for Medium-Range Weather Forecasts (ECMWF) and Copernicus Climate Change Service (C3S) (https://cds.climate.copernicus.eu/cdsapp#!/dataset/reanalysis-era5-single-levels?tab=form) are also acknowledged for providing the fifth generation data set of ECMWF atmospheric reanalysis of the global climate (ERA5).

References

Ahn, Y. W., Lachapelle, G., Skone, S., Gutman, S., & Sahm, S. (2006). Analysis of GPS RTK performance using external NOAA tropospheric corrections integrated with a multiple reference station approach. *GPS Solutions*, *10*(3), 171–186. https://doi.org/10.1007/s10291-005-0017-1

Akoglu, H. (2018). User's guide to correlation coefficients. *Turkish Journal of Emergency Medicine*, *18*(3), 91–93. https://doi.org/10.1016/j.tjem.2018.08.001

Allison, T., Fuelberg, H., & Heath, N. (2018). Simulations of vertical water vapor transport for TC Ingrid (2013). *Journal of Geophysical Research: Atmosphere*, *123*(15), 8255–8282. https://doi.org/10.1029/2018JD028334

Andersson, E., Bauer, P., Beljaars, A., Chevallier, F., Hólm, E., Janisková, M., et al. (2005). Assimilation and modeling of the atmospheric hydrological cycle in the ECMWF forecasting system. *Bulletin of the American Meteorological Society*, *86*(3), 387–402. https://doi.org/10.1175/BAMS-86-3-387

Bao, X., Wu, D., Lei, X., Ma, L., Wang, D., Zhao, K., & Jou, B. J.-D. (2017). Improving the extreme rainfall forecast of Typhoon Morakot (2009) by assimilating radar data from Taiwan Island and mainland China. *Journal of Meteorological Research*, *31*(4), 747–766. https://doi.org/10.1007/s13351-017-6007-8

Bhatia, K. T., Vecchi, G. A., Knutson, T. R., Murakami, H., Kossin, J., Dixon, K. W., & Whitlock, C. E. (2019). Recent increases in tropical cyclone intensification rates. *Nature Communications*, *10*(1), 635. https://doi.org/10.1038/s41467-019-08471-z

Blanco-Delgado, N., Duarte Nunes, F., & Seco-Granados, G. (2017). On the relation between GDOP and the volume described by the user-to-satellite unit vectors for GNSS positioning. *GPS Solutions*, *21*(3), 1139–1147. https://doi.org/10.1007/s10291-016-0592-3

Blewitt, G. (1989). Carrier phase ambiguity resolution for the Global Positioning System applied to geodetic baselines up to 2000 km. *Journal of Geophysical Research*, *94*(B8), 10187–10203. https://doi.org/10.1029/JB094iB08p10187

Copernicus Climate Change Service (C3S) (2017). *ERA5: Fifth generation of ECMWF atmospheric reanalyzes of the global climate*. Copernicus Climate Change Service Climate Data Store (Cds). https://cds.climate.copernicus.eu/cdsapp#!/home

Courtier, P., Thépaut, J.-N., & Hollingsworth, A. (1994). A strategy for operational implementation of 4D-Var, using an incremental approach. *Quarterly Journal of the Royal Meteorological Society*, *120*(519), 1367–1387. https://doi.org/10.1002/qj.49712051912

Dach, R., Lutz, S., Walser, P., & Fridez, P. (2015). *Bernese GNSS Software version 5.2, User manual*. Astronomical Institute, University of Bern, Bern Open Publishing. Retrieved from https://doi.org/10.7892/boris.72297

Dodson, A. H., Shardlow, P. J., Hubbard, L. C. M., Elgered, G., & Jarlemark, P. O. J. (1996). Wet tropospheric effects on precise relative GPS height determination. *Journal of Geodesy*, *70*(4), 188–202. https://doi.org/10.1007/BF00873700

Dong, D., & Bock, Y. (1989). Global Positioning System Network analysis with phase ambiguity resolution applied to crustal deformation studies in California. *Journal of Geophysical Research*, *94*(B4), 3949–3966. https://doi.org/10.1029/JB094iB04p03949

Dow, J. M., Neilan, R. E., & Rizos, C. (2009). The international GNSS service in a changing landscape of global navigation satellite systems. *Journal of Geodesy*, *83*, 191–198. https://doi.org/10.1007/s00190-008-0300-3

Emanuel, K. (2005). Increasing destructiveness of tropical cyclones over the past 30 years. *Nature*, *436*(7051), 686–688. https://doi.org/10.1038/nature03906

Fudeyasu, H., Ichiyanagi, K., Sugimoto, A., Yoshimura, K., Ueta, A., Yamanaka, M. D., & Ozawa, K. (2008). Isotope ratios of precipitation and water vapor observed in Typhoon Shanshan. *Journal of Geophysical Research*, *113*(D12). https://doi.org/10.1029/2007JD009313

Garbuny, M. (1965). *Optical physics - Max Garbuny*. New York, NY. Academic Press.

Geiger, A. (1988). *Atmospheric refraction and other important biases in GPS carrier phase observations*. In Atmospheric effects on geodetic space measurements, Monograph no. 12 (p. 1543).

Gordon, W. E. (1987). The propagation of radio waves: The theory of radio waves of low power in the ionosphere and magnetosphere. *Eos, Transactions – American Geophysical Union*, *68*(12), 164–165. https://doi.org/10.1029/EO068i012p00164-03

Han, H., & Wang, J. (2017). Robust GPS/BDS/INS tightly coupled integration with atmospheric constraints for long-range kinematic positioning. *GPS Solutions*, *21*(3), 1285–1299. https://doi.org/10.1007/s10291-017-0612-y

Hanisco, T. F., Moyer, E. J., Weinstock, E. M., Clair, S. J. M., Sayres, D. S., Smith, J. B., et al. (2007). Observations of deep convective influence on stratospheric water vapor and its isotopic composition. *Geophysical Research Letters*, *34*(4). https://doi.org/10.1029/2006GL027899

Hegglin, M. I., Plummer, D. A., Shepherd, T. G., Scinocca, J. F., Anderson, J., Froidevaux, L., et al. (2014). Vertical structure of stratospheric water vapor trends derived from merged satellite data. *Nature Geoscience*, *7*(10), 768–776. https://doi.org/10.1038/ngeo2236

Hersbach, H., Bell, B., Berrisford, P., Hirahara, S., Horányi, A., Muñoz-Sabater, J., et al. (2020). The ERA5 global reanalysis. *Quarterly Journal of the Royal Meteorological Society*, *146*(730), 1999–2049. https://doi.org/10.1002/qj.3803

Hersbach, H., Bell, W., Berrisford, P., Horányi, A., Muñoz-Sabater, J., Nicolas, J., et al. (2019). Global reanalysis: Goodbye ERA-Interim, hello ERA5 (Vol. 159). ECMWF Newsletter. Retrieved from https://www.ecmwf.int/node/19027

Hoffman, R. N., & Grassotti, C. (1996). A technique for assimilating SSM/I observations of marine atmospheric storms: Tests with ECMWF analyses. *Journal of Applied Meteorology*, *35*(8), 1177–1188. https://doi.org/10.1175/1520-0450(1996)035<1177:ATFASO>2.0.CO;2

Hong Kong Observatory (2019). *Tropical cyclones in 2017* (pp. 86–125). Hong Kong: Hong Kong Observatory. Retrieved from https://www.hko.gov.hk/publica/tc/TC2017.pdf

Hopfield, H. S. (1969). Two-quartic tropospheric refractivity profile for correcting satellite data. *Journal of Geophysical Research*, *74*(18), 4487–4499. https://doi.org/10.1029/JC074i018p04487

Hopfield, H. S. (1971). Tropospheric effect on electromagnetically measured range: Prediction from surface weather data. *Radio Science*, *6*(3), 357–367. https://doi.org/10.1029/RS006i003p00357

Hu, B., Chen, J., & Zhang, X. (2019). Monitoring the land subsidence area in a coastal urban area with InSAR and GNSS. *Sensors*, *19*(14), 3181. https://doi.org/10.3390/s19143181

Hwang, C., Yang, Y., Kao, R., Han, J., Shum, C. K., Galloway, D. L., et al. (2016). Time-varying land subsidence detected by radar altimetry: California, Taiwan, and north China. *Scientific Reports*, *6*(1), 28160. https://doi.org/10.1038/srep28160

Ke, F., Wang, J., Tu, M., Wang, X., Wang, X., Zhao, X., & Deng, J. (2019). Characteristics and coupling mechanism of GPS ionospheric scintillation responses to the tropical cyclones in Australia. *GPS Solutions*, *23*(2), 34. https://doi.org/10.1007/s10291-019-0826-2

Knapp, K. R., Kruk, M. C., Levinson, D. H., Diamond, H. J., & Neumann, C. J. (2010). The International Best Track Archive for Climate Stewardship (IBTrACS). *Bulletin of the American Meteorological Society*, *91*(3), 363–376. https://doi.org/10.1175/2009BAMS2755.1

Kouba, J., & Héroux, P. (2001). Precise Point positioning using IGS orbit and clock products. *GPS Solutions*, *5*(2), 12–28. https://doi.org/10.1007/PL00012883

Lagler, K., Schindelegger, M., Böhm, J., Krásná, H., & Nilsson, T. (2013). GPT2: Empirical slant delay model for radio space geodetic techniques. *Geophysical Research Letters*, *40*(6), 1069–1073. https://doi.org/10.1002/grl.50288

Landsea, C. W. (2005). Hurricanes and global warming. *Nature*, *438*(7071), E11–E12. https://doi.org/10.1038/nature04477

Larnier, H., Sailhac, P., & Chambodut, A. (2017). Detection and characterization of lightning-based sources using continuous wavelet transform: Application to audio-magnetotellurics. *Geophysical Journal International*, *212*(1), 103–118. https://doi.org/10.1093/gji/ggx418

Lawrence, D., Langley, R. B., Kim, D., Chan, F.-C., & Pervan, B. (2006). *Decorrelation of troposphere across short baselines*. Paper presented at Coronado, CA. 2006 IEEE/ION Position, Location, and Navigation Symposium (pp. 94–102). https://doi.org/10.1109/PLANS.2006.1650592

Lawrence, H., Bormann, N., Geer, A. J., Lu, Q., & English, S. J. (2018). Evaluation and assimilation of the microwave sounder MWHS-2 onboard FY-3C in the ECMWF numerical weather prediction system. *IEEE Transactions on Geoscience and Remote Sensing*, *56*(6), 3333–3349. https://doi.org/10.1109/TGRS.2018.2798292

Leandro, R. F., Langley, R. B., & Santos, M. C. (2008). UNB3m_pack: A neutral atmosphere delay package for radiometric space techniques. *GPS Solutions*, *12*(1), 65–70. https://doi.org/10.1007/s10291-007-0077-5

Leandro, R. F., Santos, M. C., & Langley, R. B. (2006). UNB neutral atmosphere models: Development and performance. Paper presented at 2006 ION NTM (Vol. 52, pp. 564–573). Monterey, CA.

Li, B., Zhang, Z., Zang, N., & Wang, S. (2019). High-precision GNSS ocean positioning with BeiDou short-message communication. *Journal of Geodesy*, *93*(2), 125–139. https://doi.org/10.1007/s00190-018-1145-z

Liu, Y., San Liang, X., & Weisberg, R. H. (2007). Rectification of the bias in the wavelet power spectrum. *Journal of Atmospheric and Oceanic Technology*, *24*(12), 2093–2102. https://doi.org/10.1175/2007JTECHO511.1

Lu, C., Zus, F., Ge, M., Heinkelmann, R., Dick, G., Wickert, J., & Schuh, H. (2016). Tropospheric delay parameters from numerical weather models for multi-GNSS precise positioning. *Atmospheric Measurement Techniques*, *9*(12), 5965–5973. https://doi.org/10.5194/amt-9-5965-2016

Macalalad, E. P., Tsai, L.-C., & Wu, J. (2016). Performance evaluation of different ionospheric models in single-frequency code-based differential GPS positioning. *GPS Solutions*, *20*(2), 173–185. https://doi.org/10.1007/s10291-014-0422-4

Makarieva, A. M., Gorshkov, V. G., Nefiodov, A. V., Chikunov, A. V., Sheil, D., Nobre, A. D., & Li, B.-L. (2017). Fuel for cyclones: The water vapor budget of a hurricane as dependent on its movement. *Atmospheric Research*, *193*, 216–230. https://doi.org/10.1016/j.atmosres.2017.04.006

Marks, F. D. (2015). Tropical cyclones and hurricanes: Observation. In North, G. R., Pyle, J., & Zhang, F. (Eds.), *Encyclopedia of atmospheric Sciences* (2nd ed., pp. 35–56).Oxford: Academic Press. https://doi.org/10.1016/B978-0-12-382225-3.00163-8

Mateus, P., Miranda, P. M. A., Nico, G., Catalão, J., Pinto, P., & Tomé, R. (2018). Assimilating InSAR maps of water vapor to improve heavy rainfall forecasts: A case study with two successive storms. *Journal of Geophysical Research: Atmosphere*, *123*(7), 3341–3355. https://doi.org/10.1002/2017JD027472

Meng, F., Wang, S., & Zhu, B. (2015). GNSS reliability and positioning accuracy enhancement based on fast satellite selection algorithm and RAIM in multiconstellation. *IEEE Aerospace and Electronic Systems Magazine*, *30*(10), 14–27. https://doi.org/10.1109/MAES.2015.140024

Nenadic, Z., & Burdick, J. W. (2005). Spike detection using the continuous wavelet transform. *IEEE Transactions on Biomedical Engineering*, *52*(1), 74–87. https://doi.org/10.1109/TBME.2004.839800

Nolan, D. S., & Zhang, J. A. (2017). Spiral gravity waves radiating from tropical cyclones. *Geophysical Research Letters*, *44*(8), 3924–3931. https://doi.org/10.1002/2017GL073572

Saastamoinen, J. (1972). *Atmospheric correction for the troposphere and stratosphere in radio ranging satellites*. In The Use of Artificial Satellites for Geodesy (Vol. 15, pp. 247–251). https://doi.org/10.1029/GM015p0247

Sadowsky, J. (1994). The continuous wavelet transform: A tool for signal investigation and understanding. *Johns Hopkins APL Technical Digest*, *15*, 306–318.

Santerre, R., & Geiger, A. (2018). Geometry of GPS relative positioning. *GPS Solutions*, *22*(2), 50. https://doi.org/10.1007/s10291-018-0713-2

Shi, L., Olabarrieta, M., Nolan, D. S., & Warner, J. C. (2020). Tropical cyclone rainbands can trigger meteotsunamis. *Nature Communications*, *11*(1), 678. https://doi.org/10.1038/s41467-020-14423-9

Simmons, A., Soci, C., Nicolas, J., Bell, B., Berrisford, P., Dragani, R., et al. (2020). *Global stratospheric temperature bias and other stratospheric aspects of ERA5 and ERA5.1*. ECMWF Technical Memoranda. Retrieved from https://www.ecmwf.int/node/19362

Sinha, S., Routh, P. S., Anno, P. D., & Castagna, J. P. (2005). Spectral decomposition of seismic data with continuous-wavelet transform. *Geophysics*, *70*(6), P19–P25. https://doi.org/10.1190/1.2127113

Smith, E. K., & Weintraub, S. (1953). The constants in the equation for atmospheric refractive index at radio frequencies. *Proceedings of the IRE*, *41*(8), 1035–1037. https://doi.org/10.1109/JRPROC.1953.274297

Subrahmanyam, K. V., Kumar, K. K., & Tourville, N. D. (2018). CloudSat observations of three-dimensional distribution of cloud types in tropical cyclones. *IEEE Journal of Selected Topics in Applied Earth Observations and Remote Sensing*, *11*(2), 339–344. https://doi.org/10.1109/JSTARS.2017.2786666

Takasu, T. (2011). *RTKLIB: An open source program package for GNSS positioning* (Tech. Rep. 2013). Software and Documentation.

Torrence, C., & Compo, G. P. (1998). A practical guide to wavelet analysis. *Bulletin of the American Meteorological Society*, *79*(1), 61–78. https://doi.org/10.1175/1520-0477(1998)079<0061:APGTWA>2.0.CO;2

Tregoning, P., & Herring, T. A. (2006). Impact of a priori zenith hydrostatic delay errors on GPS estimates of station heights and zenith total delays. *Geophysical Research Letters*, *33*(23). https://doi.org/10.1029/2006GL027706

Tunalı, E., & Özlüdemir, M. T. (2019). GNSS PPP with different troposphere models during severe weather conditions. *GPS Solutions*, *23*(3), 82. https://doi.org/10.1007/s10291-019-0874-7

Vaclavovic, P., Dousa, J., Elias, M., & Kostelecky, J. (2017). Using external tropospheric corrections to improve GNSS positioning of hot-air balloon. *GPS Solutions*, *21*(4), 1479–1489. https://doi.org/10.1007/s10291-017-0628-3

Wang, J., & Liu, Z. (2019). Improving GNSS PPP accuracy through WVR PWV augmentation. *Journal of Geodesy*, *93*(9), 1685–1705. https://doi.org/10.1007/s00190-019-01278-2

Wang, M., Ren, F., Xie, Y., Li, G., Yang, M. -J., & Feng, T. (2020). Characteristics and Causes of Extreme Rainfall Induced by Binary Tropical Cyclones over China. *Asia-Pacific Journal of Atmospheric Sciences*, https://doi.org/10.1007/s13143-020-00201-6

Wang, Y., Liu, Z., Yang, S., Min, J., Chen, L., Chen, Y., & Zhang, T. (2018). Added value of assimilating Himawari-8 AHI water vapor radiances on analyses and forecasts for "7.19" severe storm over north China. *Journal of Geophysical Research: Atmosphere*, *123*(7), 3374–3394. https://doi.org/10.1002/2017JD027697

Wang, Z., & Hankes, I. (2016). Moisture and precipitation evolution during tropical cyclone formation as revealed by the SSM/I–SSMIS retrievals. *Journal of the Atmospheric Sciences*, *73*(7), 2773–2781. https://doi.org/10.1175/JAS-D-15-0306.1

Weng, H., & Lau, K.-M. (1994). Wavelets, period doubling, and time–frequency localization with application to organization of convection over the tropical Western Pacific. *Journal of the Atmospheric Sciences*, *51*(17), 2523–2541. https://doi.org/10.1175/1520-0469(1994)051<2523:WPDATL>2.0.CO;2

Wielgosz, P., Paziewski, J., & Baryła, R. (2011). On constraining zenith tropospheric delays in processing of local GPS networks with Bernese Software. *Survey Review*, *43*(323), 472–483. https://doi.org/10.1179/003962611X13117748891877

Wilgan, K., & Geiger, A. (2018). High-resolution models of tropospheric delays and refractivity based on GNSS and numerical weather prediction data for alpine regions in Switzerland. *Journal of Geodesy*, *93*(6), 819–835. https://doi.org/10.1007/s00190-018-1203-6

Wilgan, K., Hadas, T., Hordyniec, P., & Bosy, J. (2017). Real-time precise point positioning augmented with high-resolution numerical weather prediction model. *GPS Solutions*, *21*(3), 1341–1353. https://doi.org/10.1007/s10291-017-0617-6

Won, J., & Kim, D. (2015). Analysis of temporal and spatial variation of precipitable water vapor according to path of typhoon EWINIAR using GPS permanent stations. *Journal of Positioning, Navigation, and Timing*, *4*(2), 87–95. https://doi.org/10.11003/JPNT.2015.4.2.087

Yamaguchi, M., Chan, J. C. L., Moon, I.-J., Yoshida, K., & Mizuta, R. (2020). Global warming changes tropical cyclone translation speed. *Nature Communications*, *11*(1), 47. https://doi.org/10.1038/s41467-019-13902-y

Yang, Z., & Liu, Z. (2016). Observational study of ionospheric irregularities and GPS scintillations associated with the 2012 tropical cyclone Tembin passing Hong Kong. *Journal of Geophysical Research: Space Physics*, *121*(5), 4705–4717. https://doi.org/10.1002/2016JA022398

Yeh, T.-K., Hong, J.-S., Wang, C.-S., Chen, C.-H., Chen, K.-H., & Fong, C.-T. (2016). Determining the precipitable water vapor with ground-based GPS and comparing its yearly variation to rainfall over Taiwan. *Advances in Space Research*, *57*(12), 2496–2507. https://doi.org/10.1016/j.asr.2016.04.002

Yu, C.-K., Lin, C.-Y., Cheng, L.-W., Luo, J.-S., Wu, C.-C., & Chen, Y. (2018). The degree of prevalence of similarity between outer tropical cyclone rainbands and squall lines. *Scientific Reports*, *8*(1), 8247. https://doi.org/10.1038/s41598-018-26553-8

Zahn, A., Christner, E., van Velthoven, P. F. J., Rauthe-Schöch, A., & Brenninkmeijer, C. A. M. (2014). Processes controlling water vapor in the upper troposphere/lowermost stratosphere: An analysis of 8 years of monthly measurements by the IAGOS-CARIBIC observatory. *Journal of Geophysical Research: Atmosphere*, *119*(19), 505–511. https://doi.org/10.1002/2014JD021687

Zhao, J., Zhan, R., & Wang, Y. (2018). Global warming hiatus contributed to the increased occurrence of intense tropical cyclones in the coastal regions along East Asia. *Scientific Reports*, *8*(1), 6023. https://doi.org/10.1038/s41598-018-24402-2

Zhou, Z., & Li, B. (2017). Optimal Doppler-aided smoothing strategy for GNSS navigation. *GPS Solutions*, *21*(1), 197–210. https://doi.org/10.1007/s10291-015-0512-y

Zou, X., Wang, Y., Deng, C., Tang, W., Li, Z., Cui, J., et al. (2017). Instantaneous BDS + GPS undifferenced NRTK positioning with dynamic atmospheric constraints. *GPS Solutions*, *22*(1), 17. https://doi.org/10.1007/s10291-017-0668-8

Zumberge, J. F., Heflin, M. B., Jefferson, D. C., Watkins, M. M., & Webb, F. H. (1997). Precise point positioning for the efficient and robust analysis of GPS data from large networks. *Journal of Geophysical Research*, *102*(B3), 5005–5017. https://doi.org/10.1029/96JB03860

Zwillinger, D. (2002). *CRC standard mathematical tables and formulae*. Washington, DC: CRC Press.